Splitting of a three-dimensional liquid plug at an airway bifurcation

Hideki Fujioka,[1,a] (iD) Francesco Romanò,[2] (iD) Metin Muradoglu,[3] (iD) and James B. Grotberg[4] (iD)

AFFILIATIONS

[1]Center for Computational Science, Tulane University, 6823 St. Charles Avenue, New Orleans, Louisiana 70118, USA

[2]Univ. Lille, CNRS, ONERA, Arts et Métiers Institute of Technology, Centrale Lille, UMR 9014-LMFL-Laboratoire de Mécanique des Fluides de Lille–Kampé de Fériet, F-59000 Lille, France

[3]Department of Mechanical Engineering, Koc University, Rumelifeneri Yolu Sariyer/Istanbul 34450, Turkey

[4]Department of Biomedical Engineering, University of Michigan, 2200 Bonisteel Blvd., Ann Arbor, Michigan 48109, USA

[a]Author to whom correspondence should be addressed: fuji@tulane.edu

ABSTRACT

Employing the moving particles' semi-implicit (MPS) method, this study presents a numerical framework for solving the Navier–Stokes equations for the propagation and the split of a liquid plug through a three-dimensional air-filled bifurcating tube, where the inner surface is coated by a thin fluid film, and surface tension acts on the air–liquid interface. The detailed derivation of a modified MPS method to handle the air–liquid interface of liquid plugs is presented. When the front air–liquid interface of the plug splits at the bifurcation, the interface deforms quickly and causes large wall shear stress. We observe that the presence of a transverse gravitational force causes asymmetries in plug splitting, which becomes more pronounced as the capillary number decreases or the Bond number increases. We also observe that there exists a critical capillary number below which the plug does not split into two daughter tubes but propagates into the lower daughter tube only. In order to deliver the plug into the upper daughter tube, the driving pressure to push the plug is required to overcome the hydrostatic pressure due to gravity. These tendencies agree with our previous experimental and theoretical studies.

I. INTRODUCTION

Liquid is instilled into the pulmonary airways in some medical treatments such as surfactant replacement therapy (SRT),[1–6] partial liquid ventilation,[7–11] and drug delivery.[12–16] Liquid delivery to the targeted areas of the lung is important for achieving successful results in such treatments. A strategy to deliver a small liquid bolus to the distal airways is to create a liquid plug at an upper airway and push it into the descending airways by air flow. The formation of a liquid plug in the trachea, prior to inspiration, is important to create a more uniform distribution of liquid throughout the lung than with gravitational drainage alone.[17,18] A high ventilation rate results in a more homogeneous liquid plug delivery.[19] Liquid plugs are formed in large airways by faster instillation rates of perfluorocarbons into the trachea.[20] In addition to liquid delivery, airway closure due to plug formation and reopening from plug propagation and rupture can be a source of airway injury.[21] Coronavirus disease-19 (COVID-19) can cause lung complications such as pneumonia and, in the most severe cases, acute respiratory distress syndrome (ARDS).[22] In pneumonia, the lungs become filled with fluid and inflamed, leading to breathing difficulties as well as lung injury due to plug formation.

In order to gain a better understanding of how plugs are used effectively in medical treatments and how a plug behaves once it is created, it is important to understand how the dynamics of liquid plugs is affected by the properties of fluids and the geometry of the airways. As the liquid plug propagates through the airways, it leaves the trailing liquid film on the inner surface of the airways and splits at the airway bifurcations. The trailing film thickness and the split ratio are functions of the physical properties of the liquid (viscosity, density, surface tension at the air/liquid interface, surfactant concentration), the direction of gravity, the bifurcation geometry, the precursor liquid film thickness ahead of the plug, the initial plug volume, the plug propagation speed, airway wall elasticity, and uneven flow resistance of two daughter tubes at the bifurcation. We need to understand the effect of these factors on achieving homogeneous liquid delivery to the lungs. The flow of the liquid plug was analytically modeled by Howell et al.,[23] Waters and Grotberg[24] with surfactant, and Suresh and Grotberg[25] with gravity. Mamba et al.[26] investigated both experimentally and theoretically the dynamics of a liquid plug driven by a cyclic force inside a rigid capillary tube. Computational modeling of the propagation of the liquid plug in a tube/channel has been performed using the finite

volume method with the body-fit mesh,[27–30] the finite element method with the body-fit mesh,[31,32] the sharp interface method,[33] the volume-of-fluids (VOF) method,[34] and the multiphase lattice Boltzmann method.[35] The creation of liquid plugs as a consequence of airway closure was simulated by Romanò et al.[36] using the level-set method.

Zheng et al.[37,38] experimentally investigated the effect of gravity on the splitting of the liquid plug in a symmetrical bifurcating tube model. They showed that plug splitting became more uneven for smaller capillary number (Ca) and larger Bond numbers (Bo). $Ca = \mu U/\sigma$ is the ratio of viscous force to surface tension, and $Bo = \rho g L^2/\sigma$ is the ratio of the gravitational force to surface tension, where μ and ρ are the viscosity and the density of fluid, σ is the surface tension, and U and L are characteristic velocity and length scales. They proposed a simple one-dimensional model for the splitting ratio as a function of the bifurcation orientations with respect to the gravity, Ca, and Bo. Copploe et al.[39] developed a bioengineering approach to design three-dimensional bifurcating airway models using morphometric data from human lung and experimentally examined the dynamics of liquid plug splitting in fabricated physical bifurcation models. Filoche et al.[40,41] used the one-dimensional mathematical model to develop a three-dimensional lung airway model of SRT and compared it to experiments with rats' lungs.[42] Vaughan and Grotberg[43] used the finite element method and investigated the split process of a liquid plug by a two-dimensional bifurcation model under the influence of a transverse gravitational field and showed qualitative agreement with Zheng et al.[37]

During liquid plug splitting at bifurcation, the air–liquid interface contracts/stretches, and breaks/merges. There are some computational methods that can handle large deformations and topological changes in interfaces. The interface-tracking methods compute the flow on an Eulerian, usually fixed grid, while a set of Lagrangian markers is used to define the interface.[33,34,44,45] Volume-of-fluid (VOF) methods[46] and level set methods[47] are interface capturing methods, where the interface is not tracked explicitly. They use a transport of fraction, level-set, or phase-field function to capture interfaces. Smoothed particle hydrodynamics (SPH) and the moving particle semi-implicit (MPS) methods[48] are in the category of particle methods. Both methods are a full Lagrangian meshless method. Essentially, the computational volume/area is discretized by particles. Therefore, mass conservation is achieved precisely. Both methods can handle complex geometries and topological changes in the interface. The SPH method has been developed initially for astrophysical problems and has recently been applied to fluid dynamics with weak compressibility. The MPS method has been developed to solve incompressible and interfacial flows. The major difference from SPH is that the MPS method solves pressure fields implicitly, where the governing equations are transformed based on particle representations, resulting in a Poisson equation for pressure.

In this study, we investigated the effect of gravity on the splitting of the liquid plug in a three-dimensional bifurcating airway model employing the moving particles semi-implicit (MPS) method.[48] The method can simulate the physical process from pre- to post-split phases. The previous numerical study[43] was limited to the bulk fluid split process, which did not cover the topological changes of the air–liquid interfaces.

In Sec. II, the numerical method is presented. In Sec. II A, our use of the MPS method for two-phase flow is outlined. In Sec. II B, our three-dimensional bifurcating tube model is described. In Sec. II C, the governing equations are presented. In Sec. II D, the numerical procedures are presented. In Sec. III, our computational results and discussions are presented. Conclusions and future work are given in Sec. IV.

II. METHOD

We investigate the propagation and split of a liquid plug in a three-dimensional bifurcating tube model. The Navier–Stokes equation coupled with the force balance due to the surface tension on the air–liquid interface is solved by using the MPS method.[48] In the MPS method, the computational domain is discretized with a number of particles. Figure 1 schematically shows the discretization of the model rigid wall and the fluid, which are represented by three types of particles. The rigid wall consists of the wall and the ghost particles, which are immobile, thus the velocities of these particles are set to zero. The fluid particles, which are composed of liquid and air particles, are allowed to move with their velocities. In Fig. 1, $\{\Pi_W\}$, $\{\Pi_G\}$, and $\{\Pi_F\}$ denote the group of wall, ghost, and fluid particles, respectively. Particles within a distance of r_e from the inlet/outlet boundary, which is grouped into $\{\Pi_{We}\}$ and $\{\Pi_{Fe}\}$, must be treated differently from the normal particles, which are grouped into $\{\Pi_{Wn}\}$ and $\{\Pi_{Fn}\}$. r_e is the size of the weight function, which is explained below.

In this study, we consider flow through a tube whose inlet and outlet are not periodic boundaries. Therefore, when the fluid particles exit the outlet, x_{B1}, they are removed. When the inlet particles move into the interior fluid domain, the type of particles is changed to the normal fluid particle. The particles are placed in cells of the empty inlet grid and the type of the particles is set to the inlet particle.

A. MPS method

The MPS method was first introduced by Koshizuka and Oka[48] and their research group and is used by many other researchers. Each particle is a node point where the flow variables such as velocity vector, pressure, and concentration of some species are computed. Particles move with their velocity carrying these variables. The spatial derivatives are computed using neighboring particles. The details are presented in Appendix B. The particle number density is an important quantity, which is defined at the location of particle i as

$$\psi_i = \sum_{j \neq i}^{N} w(||\mathbf{x}_j - \mathbf{x}_i||), \tag{1}$$
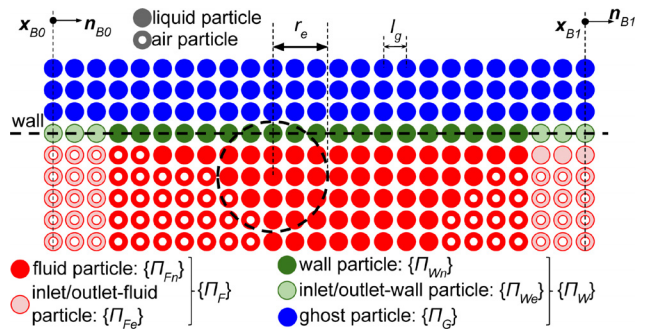

FIG. 1. Particle types in a tube domain. There are three types of particles representing the fluid, the wall, and ghost domains. The fluid particles comprise of liquid and air particles. The wall and ghost particles are immobile.

where N is all neighboring particles of any type, and $w(r)$ is the weight function, which should be a monotonically decreasing function of r. In this study, we use

$$w(r) = \begin{cases} 1 - 6\left(\dfrac{r}{r_e}\right)^2 + 6\left(\dfrac{r}{r_e}\right)^3, & r < \dfrac{r_e}{2} \\[2ex] 2\left(1 - \dfrac{r}{r_e}\right)^3, & \dfrac{r_e}{2} \le r < r_e \\[2ex] 0, & r \ge r_e, \end{cases} \quad (2)$$

where r_e is a cutoff radius, which is $r_e = 2.1 \cdot l_g$ in this study, and l_g is the characteristic distance of two closest particles and is called the grid size (see Fig. 1). With $r_e = 2.1 \cdot l_g$, the number of neighborhood particles, N is approximately 40, which is larger than typical low-order mesh-based methods. The particles must be evenly distributed throughout the domain for incompressible fluids, which means that the particle number density must be constant at ψ^0.

We consider a two-phase flow that consist of liquid and air, as shown in Fig. 1. The particles that belong to the liquid phase have color number $f_i = 0$ and the particles that belong to the air phase have $f_i = 1$. The color function is defined as the weighted average of f_i as

$$c_i = \frac{\sum\limits_{j \ne i} f_j w\left(||\mathbf{x}_j - \mathbf{x}_i||\right)}{\sum\limits_{j \ne i} w\left(||\mathbf{x}_j - \mathbf{x}_i||\right)}. \quad (3)$$

The value of c_i is 0 in the liquid phase and 1 in the air phase, respectively, at far enough apart from the interface. In the vicinity of the interface, there is a transition region, where c_i changes from 0 to 1. In this study, c_i is used to determine the unit normal on the air–liquid interface, $\mathbf{n}_S$ as

$$\mathbf{n}_S = \frac{\nabla c_i}{||\nabla c_i||}, \quad (4)$$

and an approximation of Dirac's delta function, δ_S is defined as

$$\delta_S = ||\nabla c_i||, \quad (5)$$

where ∇c_i is computed by the gradient model given by Eq. (B1) in Appendix B. The wall and ghost particles are included in this calculation with $f_i = 0$ that mimics hydrophilic walls, yielding zero contact angle. The viscosity and density for each particle are modified to have a continuous change across the interface as

$$\begin{aligned} \rho_i &= \rho_l + (\rho_a - \rho_l)c_i, \\ \mu_i &= \mu_l + (\mu_a - \mu_l)c_i, \end{aligned} \quad (6)$$

where ρ_l and ρ_a are densities, and μ_l and μ_a are viscosities for liquid and air, respectively.

B. Three-dimensional airway bifurcation model

Our three-dimensional bifurcating tube is similar to the model of Zheng et al.[37,38] The bifurcating tube model is built defining two tube axes, $\mathbf{x}_1$ and $\mathbf{x}_2$, as shown in Fig. 2. Each axis provides a density space around it. The bifurcation model surface is defined by an isosurface of the total density; the sum of two densities being unity. The detailed formulation of the model is presented in Appendix A. In this study,
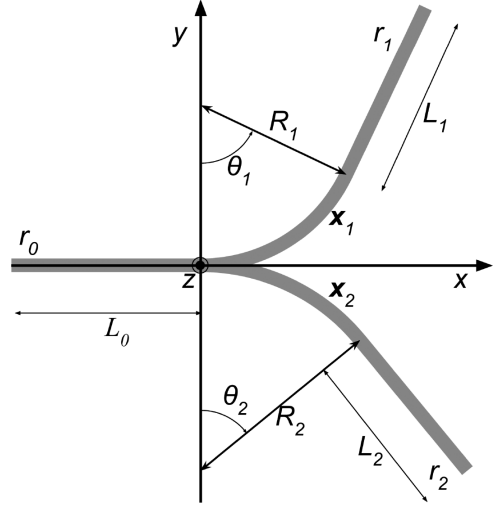

FIG. 2. Axes of bifurcating tube model. A rigid parent tube of radius r_0 bifurcates into two smaller rigid daughter tubes of radius r_1 and r_2. This branching is characterized by the total branch angle $\theta_T = \theta_1 + \theta_2$, where θ_1 and θ_2 are the branch angles for the right and left daughter tubes, respectively. The radii of the curved portion of the daughter tube axis are R_1 and R_2. $\mathbf{x}_1$ and $\mathbf{x}_2$ are the axes of the bifurcating tube, which can be divided into three regions: the parent tube, the central zone, and the daughter tubes. The two central axes merge into the single straight line of the parent tube. The details are shown in Appendix A.

we build a symmetrical bifurcation model with the parameters of $r_1 = r_2$, $r_1/r_0 = 0.78$; $\theta_1 = \theta_2 = 35°$; $R_1 = R_2$, $R_1/r_0 = 8$, where r_0 and r_1 are the radii of the parent and daughter tubes, θ_1 is the branch angle, and R_1 is the radius of curvature.[49,50] Our bifurcation model provides a smoothly varying surface curvature. We neglect small undulations on the surface and a layer of cilia of the airway wall because of numerical difficulties in including these effects.

The bifurcating tube resides within a three-dimensional gravitational field in the z direction (lab frame). We use a roll angle (θ_r) and then a pitch angle (θ_p) to define the plane orientation within this gravitational field, which is shown schematically in Fig. 3. The resulting gravitational field in the bifurcation plane is

$$\mathbf{f}_G = \rho g \begin{bmatrix} \cos\theta_r \sin\theta_p \\ -\sin\theta_r \\ -\cos\theta_r \cos\theta_p \end{bmatrix}, \quad (7)$$

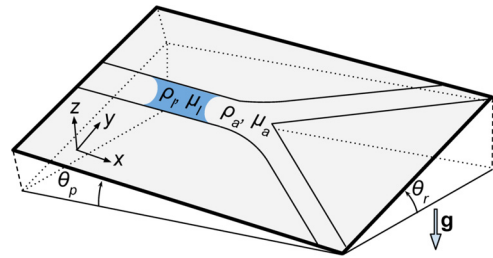FIG. 3. The orientation of model with respect to the gravity.

where g is the magnitude of gravity. For $\theta_r = \theta_p = 0°$, the gravity is only in the z direction, normal to the bifurcation plane. For $\theta_r = 90°$ and $\theta_p = 0°$, gravity is only in the y-direction, and for $\theta_r = 0°$ and $\theta_p = 90°$, gravity is only in the x direction in the frame of bifurcation plane.

C. Governing equations

In this paper, we investigate the split of a liquid plug at a bifurcating rigid tube. A pressure difference between the inlet and outlet air-phases, $\Delta P = P_{inlet} - P_{outlet}$, drives the air and liquid phases. Both phases are assumed to be Newtonian fluid, and the flow is incompressible since the velocity range considered here is $O(1)$ cm/s. The density of liquid and air are ρ_l and ρ_a, and the viscosities are μ_l and μ_a. The surface tension, σ, acts on the surface of the air–liquid interface.

With the continuum surface tension model,[51] the Navier–Stokes equation can be written as

$$\rho \frac{D\mathbf{u}}{Dt} = -\nabla p + \nabla \cdot \left[\boldsymbol{\mu}\nabla\mathbf{u} + \boldsymbol{\mu}(\nabla\mathbf{u})^{\mathbf{T}} \right] + \mathbf{f}_B, \tag{8}$$

and the continuity is

$$\frac{1}{\rho}\frac{D\rho}{Dt} + \nabla \cdot \mathbf{u} = 0. \tag{9}$$

where D/Dt is the material derivative, ρ and μ are the density and viscosity of the fluid, $\mathbf{u}$ is the velocity, p is the pressure, and $\mathbf{f}_B$ is the body force. Note that, due to incompressible flow, $D\rho/Dt = 0$. Here, we consider the gravity and the surface tension, and thus, $\mathbf{f}_B = \mathbf{f}_G + \mathbf{f}_S$, where $\mathbf{f}_S$ is the surface force density due to the surface tension. In this study, we consider only the case of constant surface tension. Therefore,

$$\mathbf{f}_S = \sigma\mathbf{n}_S\nabla \cdot \mathbf{n}_S\delta_S, \tag{10}$$

where σ is the surface tension, $\mathbf{n}_S$ is the unit normal to the air–liquid interface at $\mathbf{x}_S$, and δ_S is calculated by Eq. (5).

D. Numerical procedure

The time derivative of the momentum equation can be discretized using the Euler scheme and split into two steps as

$$\frac{D\mathbf{u}}{Dt} \simeq \frac{\mathbf{u}^{(k+1)} - \mathbf{u}^{(k)}}{\Delta t} = \frac{\mathbf{u}^{(k+1)} - \mathbf{u}^*}{\Delta t} + \frac{\mathbf{u}^* - \mathbf{u}^{(k)}}{\Delta t}, \tag{11}$$

where $\mathbf{u}^*$ is the predicted velocity and $\tilde{\mathbf{u}} = \mathbf{u}^{(k+1)} - \mathbf{u}^*$ is the velocity correction. $(k + 1)$ and (k) denote the iteration counter. The pressure gradient term is also split into $\nabla p = \nabla p^* + \rho\nabla q$, where p^* is the base pressure and q is the correction for the pressure field. The momentum equation is split into the prediction equation, which is

$$\frac{\mathbf{u}^* - \mathbf{u}^{(k)}}{\Delta t} = -\frac{1}{\rho}\nabla p^* + \frac{1}{\rho}\left[\nabla \cdot \mu(\nabla\mathbf{u}^* + \nabla\mathbf{u}^{*T}) + \mathbf{f}_B\right], \tag{12}$$

and the correction equation, which is

$$\frac{\mathbf{u}^{(k+1)} - \mathbf{u}^*}{\Delta t} = -\nabla q. \tag{13}$$

The boundary condition for the base pressure, p^*, is prescribed uniformly as P_{inlet} or P_{outlet} without considering the hydrostatic pressure distribution due to the gravity. To make this consistent, the body force

density of air, $\rho_a\mathbf{g}$, is subtracted from the momentum equation. Therefore, the gravity term Eq. (7) in Eq. (12) is modified as its density ρ replaced by $(\rho - \rho_a)$.

In this study, the velocity correction is calculated without explicitly computing the pressure. Instead, we compute q, which is equivalent to p/ρ when ρ is uniform. There is a pressure jump across the interface due to the surface tension effects. In addition, the density of the fluid changes largely at the air–liquid interface. Since the acceleration of the fluid increases with the inverse of the density at the same pressure gradient, a large density ratio causes the calculation to be unstable. For this reason, we computed q without computing the total pressure in order to eliminate the density from the velocity correction calculation.

The time derivative of the density in the continuity equation can be discretized using the Euler scheme and split into two steps as

$$\frac{1}{\rho}\frac{D\rho}{Dt} \simeq \frac{1}{\rho}\frac{\rho^{(k+1)} - \rho^*}{\Delta t} + \frac{1}{\rho}\frac{\rho^* - \rho^{(k)}}{\Delta t}. \tag{14}$$

The split continuity equations are

$$\frac{1}{\rho}\frac{\rho^* - \rho^{(k)}}{\Delta t} + \nabla \cdot \mathbf{u}^* = 0, \tag{15}$$

and

$$\frac{1}{\rho}\frac{\rho^{(k+1)} - \rho^*}{\Delta t} + \nabla \cdot \tilde{\mathbf{u}} = 0, \tag{16}$$

where $\mathbf{u}^* + \tilde{\mathbf{u}} = \mathbf{u}$ and $\mathbf{u}^*$ and $\tilde{\mathbf{u}}$ are the prediction and correction of the velocity, which are defined below.

The position and velocity of the particles are computed with the following steps.

1. Prediction step: Base pressure

In this study, the pressures are prescribed at the inlet and outlet. The first step is to compute the base pressure field that satisfies the pressure boundary conditions.[52] Applying the Laplacian model of Eq. (B3) to $\nabla^2 p^* = 0$, we obtain the linear system of equation

$$\frac{1}{\psi_i^\#} \sum_{j \neq i}^{N_F + N_W} \left[p_j^* w(||\mathbf{x}_j - \mathbf{x}_i||) \right] - p_i^* = 0, \tag{17}$$

where N_F and N_W are neighboring fluid and wall particles (see Fig. 1), $\psi_i^\# = \sum_{j \neq i}^{N_F + N_W} w(||\mathbf{x}_j - \mathbf{x}_i||)$, and $w(r)$ is the weight function defined by Eq. (2). Equation (17) is applied to normal fluid and wall particles, $\{\Pi_{F_n}\}$ and $\{\Pi_{W_n}\}$. For inlet/outlet particles, $\{\Pi_{F_e}\}$ and $\{\Pi_{W_e}\}$

$$\frac{1}{\psi^0} \sum_{j \neq i}^{N} \left[p_j^* w(||\mathbf{x}_j - \mathbf{x}_i||) \right] - p_i^* = -\frac{\psi^0 - \psi_i}{\psi^0} p_b, \tag{18}$$

is applied, where p_b is the boundary condition prescribed as P_{inlet} or P_{outlet}. ψ_i is computed by Eq. (2). Since there are no particles outside the boundary of the inlet/outlet, $\psi_i < \psi^0$ in the boundary regions.

2. Prediction step: Velocity

Using the base pressure, p^*, the predicted velocity, $\mathbf{u}^*$, is obtained by solving the momentum equation

$$\frac{\rho}{\Delta t}\mathbf{u}^* - \nabla \cdot \mu(\nabla \mathbf{u}^* + \nabla \mathbf{u}^{*T}) = \frac{\rho}{\Delta t}\mathbf{u}^{(k)} - \nabla p^* + \mathbf{f}_B. \quad (19)$$

The pressure gradient at particle i, $\langle \nabla p^* \rangle_i$, is obtained with the typical MPS scheme. We can obtain the linear system of equation and solve implicitly for $\mathbf{u}^*$, assuming $\mathbf{u}_i^{(k)} = 0$ for particles $\{\Pi_W\}$ and $\{\Pi_G\}$. The velocities at inlet/outlet particles, $\{\Pi_{F_e}\}$, are computed explicitly.

3. Prediction step: Particle position

The position of particle i with its velocity $\mathbf{u}_i^*$ is updated by

$$\mathbf{x}_i^* = \mathbf{x}_i^{(k)} + \mathbf{u}_i^* \Delta t. \quad (20)$$

Since $\mathbf{u}_i^*$ does not satisfy the continuity, this causes the particle number density to deviate from ψ^0.

When two particles are very close, the simulation becomes unstable because the particle number density is elevated locally. This will cause excessive correction values in velocity. To avoid this problem, an artificial repulsion force is added to two particles within a distance less than $0.7 \cdot l_g$ as

$$\tilde{\mathbf{f}}_i = \sum_{j \neq i}^{N} -A_{pg} \max(0.7 \cdot l_g - r, 0)(\mathbf{x}_j^* - \mathbf{x}_i^*)/r^2, \quad (21)$$

where $r = |\mathbf{x}_j^* - \mathbf{x}_i^*|$ and A_{pg} is an artificial pressure gradient; we use $A_{pg} = 100$. Adding $\tilde{\mathbf{f}}_i$ to the predicted velocity as $\tilde{\mathbf{u}}_i^* = \mathbf{u}_i^* + \tilde{\mathbf{f}}_i \Delta t$, the position of the particle i is updated again by $\mathbf{x}_i^* = \mathbf{x}_i^{(k)} + \tilde{\mathbf{u}}_i^* \Delta t$.

4. Correction step: Velocity

For incompressible flow, $\rho^{(k+1)} = \rho^{(k)} = \rho^0$. Substituting Eq. (13) into Eq. (16), we obtain the pressure correction equation as

$$\nabla^2 q = -\frac{1}{\rho}\frac{\rho^* - \rho^0}{\Delta t^2}. \quad (22)$$

Since the particle density is related to the fluid density as $\rho_i = m_i \psi_i$, where m_i is the fixed mass of the fluid particles, so $m_i = \rho_i/\psi^0$. Therefore, the above equation can be rewritten as

$$\nabla^2 q = -\frac{1}{\psi^0}\frac{\psi_i^* - \psi^0}{\Delta t^2}, \quad (23)$$

where ψ^* is the particle number density measured with the predicted position of the particles, $\mathbf{x}^*$. We discretize Eq. (23) similar to Eq. (17) with the boundary condition of $q_{inlet} = q_{outlet} = 0$, q obtained. Applying Eq. (13), the velocity of $\{\Pi_{F_n}\}$ is corrected.

5. Correction step: Position of the particle

The position of the particle i is corrected by

$$\mathbf{x}_i^{(k+1)} = \mathbf{x}_i^* + \tilde{\mathbf{u}}_i \Delta t. \quad (24)$$

The numerical method is implemented using C++ and compiled with Intel C++ compiler with Intel MPI library. PETSc library[53] is used to manage particles and solve a large linear system of equations in parallel on a distributed memory computing cluster. Also, Eigen[54] is utilized for local linear algebra. The results data are stored with HDF5[55] format. Approximately 850 000 particles are distributed in a
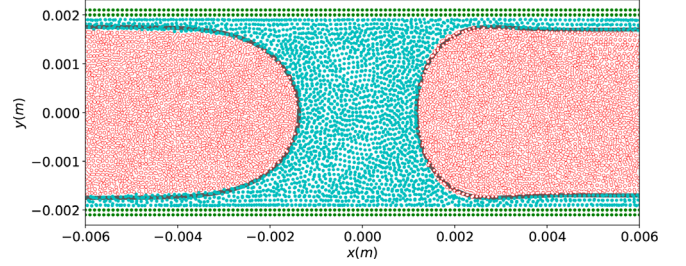

FIG. 4. Comparison of interface shape with the finite volume method result by Fujioka et al.[30] $Ca = 0.05$.

bifurcating tube model. The computations were performed mainly on eight nodes of dual 10-core 2.8 GHz Intel Xeon E5–2680 v2 CPUs system; total 160 cores for each case.

III. RESULTS AND DISCUSSION

In this study, we investigated the propagation of a liquid plug in air-filled tubes. The density and viscosity of liquid are $\rho_l = 1000 \text{ kg/m}^3$ and $\mu_l = 10^{-2} \text{ Pa s}$, and these of air are $\rho_a = 1 \text{ kg/m}^3$ and $\mu_a = 10^{-5} \text{ Pa s}$, as base values. Here, we consider the liquid as the lung fluid secreted naturally in healthy lungs and, therefore, assume μ_l to be ten times higher than the viscosity of water. We tested the effect of the liquid viscosity in a range of $6 \times 10^{-3} \leq \mu_l \leq 6 \times 10^{-2} \text{ Pa s}$. The gravitational constant is $g = 10 \text{ m/s}^2$. We varied the surface tension between the liquid and gas as $10^{-2} \leq \sigma \leq 2 \times 10^{-2} \text{ N/m}$, which is relevant to the surface tension when the pulmonary surfactant exists on the air–liquid interface. In this study, we assume a uniform surface tension though the surface tension varies as a function of the surfactant concentration. The geometry of the bifurcation model is built with the following parameters: $r_1 = r_2$, $r_1/r_0 = 0.78$, $\theta_1 = \theta_2 = 35°$, $R_1 = R_2$, $R_1/r_0 = 8$. We varied the radius of the parent tube within the range $10^{-3} \leq r_0 \leq 3 \times 10^{-3} \text{ m}$, keeping the aspect ratios fixed. These sizes are equivalent to fourth to ninth generation of the pulmonary airways.[56] The Bond number, $Bo = \rho_l g r_0^2/\sigma$, ranges between $1 \leq Bo \leq 9$. The Laplace number, $La = \rho_l \sigma r_0/\mu_l^2$, which is a ratio of surface tension to momentum transport, ranges between $8.33 \leq La \leq 833$. The capillary number, $Ca = \mu_l \bar{U}/\sigma$, which is a function of the plug speed, $\bar{U}$, ranges
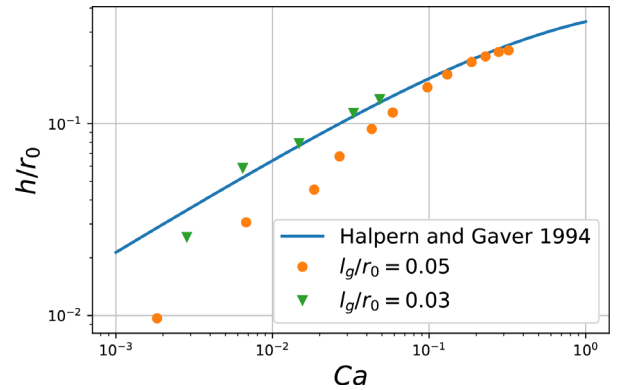

FIG. 5. Estimation of the trailing film thickness.

$Ca < 0.1$. The Reynolds number, $Re = La \cdot Ca = \rho_l r_0 \bar{U} / \mu_l$, which is a ratio of viscous force tension to momentum, ranges $Re < 60$.

A. Validations

The propagation of a liquid plug in a straight channel/tube was computed to validate the code for the two-phase flows. Figure 4 shows the distribution of air/liquid/wall particles within $|z| < 0.5 l_g$ projected onto the xy plane. The solid lines were the interface shape of the plug computed by the finite volume method with the boundary-fitted mesh.[30] The solid lines correspond well to the boundaries of the air and liquid particles.

Figure 5 demonstrates the trailing film thickness of plugs in two-dimensional channel for the particle gird size of $l_g/r_0 = 0.05$ and 0.03, compared with an empirical formula by Ref. 57. The trailing film thickness, h, is estimated from $(r_0 - h)U_{air} = r_0 \bar{U}$, where U_{air} is the averaged velocity of air particles, $\bar{U}$ is the averaged velocity of all particles, and r_0 is the tube radius. The MPS results agree reasonably well with the empirical formula. Since the film thickness is thin and close of the size of grid, there exist deviations from the empirical formula. If we used smaller size of l_g, the results would be improved but increase the computational cost. In this study, we use $l_g/r_0 = 0.05$. The estimated errors in the film thickness are within a factor of two.
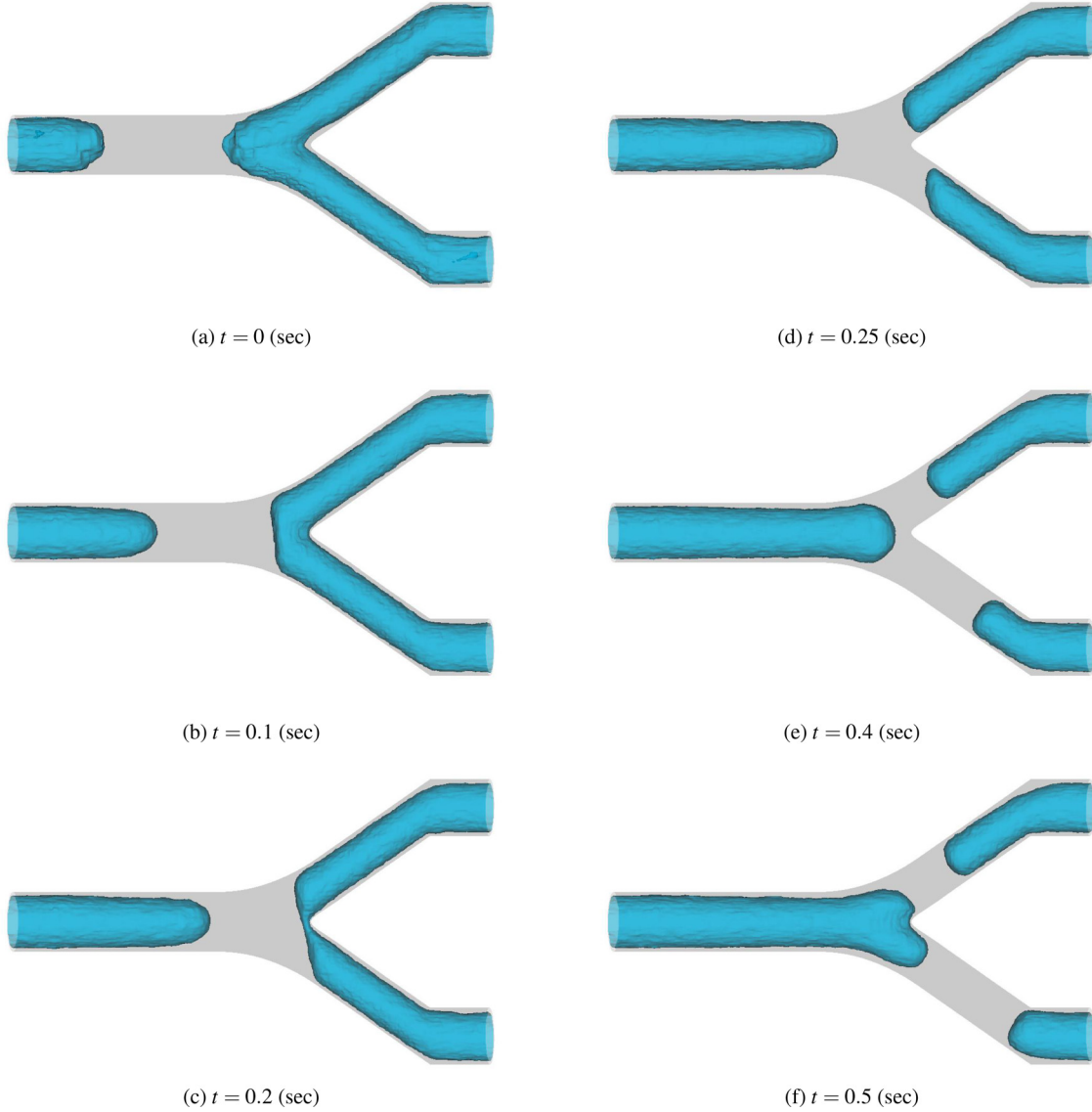

(a) $t = 0$ (sec)

(b) $t = 0.1$ (sec)

(c) $t = 0.2$ (sec)

(d) $t = 0.25$ (sec)

(e) $t = 0.4$ (sec)

(f) $t = 0.5$ (sec)

FIG. 6. Snapshots of a liquid plug splitting at a bifurcating tube. The inner surface of the bifurcating tube (gray) and the air–liquid interface (cyan) are plotted. $Bo = 4$, $La = 200$, $\theta_r = 90°$, $\theta_p = 0°$. The resultant $R_S = 0.514$, $Ca = 0.0284$, and $Re = 5.67$. (a) $t = 0$ s, (b) $t = 0.1$ s, (c) $t = 0.2$ s, (d) $t = 0.25$ s, (e) $t = 0.4$ s, and (f) $t = 0.5$ s.

B. Liquid plug split at bifurcation

Figure 6 demonstrates a liquid plug propagation and split at the bifurcating tube of $r_0 = 2 \times 10^{-3}$ m. The three-dimensional shapes of the air–liquid interface and the inner tube surfaces are constructed and projected on the two-dimensional plane. Initially, the plug of length $L_P/r_0 = 4$ is placed in the parent tube, Fig. 6(a). The pressure difference between the inlet and outlet drives the plug to propagate toward the bifurcation. The pressures at the two daughter tube outlets are zero. The parent tube inlet pressure is 20 Pa. The roll angle is $\theta_r = 90°$, and the pitch angle is $\theta_p = 0°$; thus, the gravity acts downward in the figure. The remaining non-dimensional parameters are $Bo = 4$ and $La = 200$. As the plug approaches the bifurcating section, the front interface of the plug is stretched to the direction of two bifurcating tubes, Fig. 6(b). More liquid drains into the lower branch than the upper branch due to the gravity, Fig. 6(c). After the front interface splits at the flow divider, Figs. 6(d) and 6(e), the two front interfaces quickly deform to a hemisphere-shaped shape due to the surface tension. The interface entered to the lower daughter tube moved faster because the hydrostatic pressure due to the gravity accelerates the liquid downward. The rear interface propagates and leaves a thin liquid layer on the tube wall behind. Finally, in Fig. 6(d), the rear interface is split into two daughter tubes. The trailing liquid film is thicker in the bifurcating section, where the tube cress section is large.

After the front interface is split into two daughter tubes, each front interface is transformed into a hemisphere-like shape. Figure 7 shows the particles in the vicinity of the bifurcation plane, $z = 0$ for $t = 0.21–0.24$ s, which is between (c) and (d) in Fig. 6. When the front air–liquid interface impacts against the flow divider, the liquid particles quickly move into the daughter tubes along the wall. The surface curvature near the wall becomes large, and the Laplace pressure accelerates the liquid particles along the wall. Due to the faster movement of the meniscus, the wall shear stress near the flow divider is elevated. For the case in Fig. 6, the wall shear stress increased to 3 Pa when the front meniscus split as shown in Fig. 8. This may cause damage to epithelial cells around the bifurcation carina.[58]

Due to the gravity, the plug splits unevenly as seen in Fig. 6. More liquid goes to the lower daughter tube. To quantify the unevenness of the split, the plug split ratio, R_S is calculated from the amount of liquid volume delivered to each daughter tube. Figure 9 shows the volume of liquid in the parent tube, V_{parent}, and each daughter tube, V_{upper} and V_{lower}, which are the volumes of liquid within the upper and lower daughter tube with respect to the direction of the gravity. The liquid volume was estimated from the number of liquid particles in each region; parent tube, $x < 3r_0$; upper daughter tube, $x \geq 3r_0$ and $y \geq 0$; and lower daughter tube, $x \geq 3r_0$ and $y < 0$. At the beginning, $t < 0.1$ s, the most of the liquid is in the parent tube. A small amount of liquid exists in both daughter tubes because of a thin lining
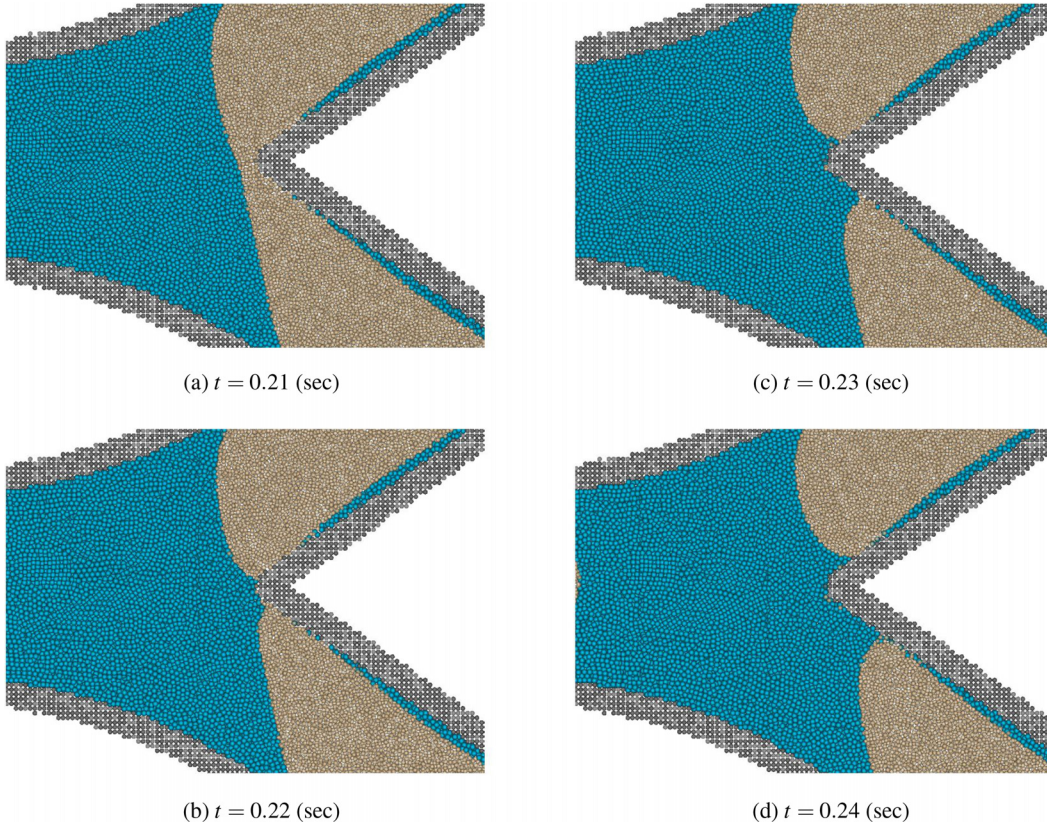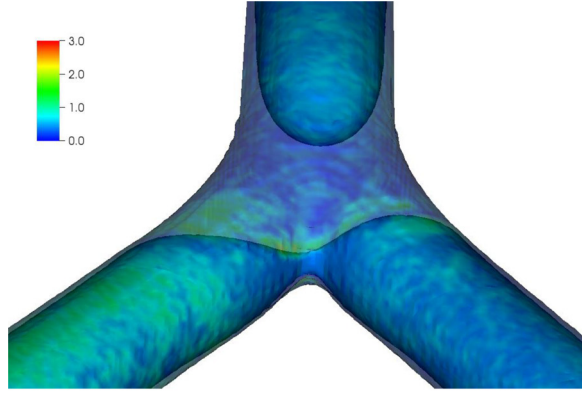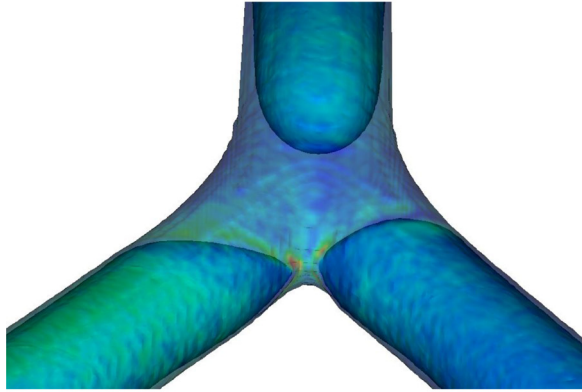

(a) $t = 0.21$ (sec)

(b) $t = 0.22$ (sec)

(c) $t = 0.23$ (sec)

(d) $t = 0.24$ (sec)

FIG. 7. Particles near $z = 0$ plane during the front meniscus of liquid plug splitting at the bifurcation carina for the case shown in Fig. 6. Liquid and air particles are represented by cyan and gray, respectively, and wall particles are represented by black. (a) $t = 0.21$ s, (b) $t = 0.22$ s, (c) $t = 0.23$ s, and (d) $t = 0.24$ s.

(a) $t = 0.21$ (sec)

(b) $t = 0.22$ (sec)

FIG. 8. The wall shear stress distribution at (a) $t = 0.21$ and (b) $t = 0.22$ s, right after the front meniscus splits at the flow divider, see Fig. 6(c).

liquid, which is initially prescribed. As the plug moves into the bifurcation, V_{upper} and V_{lower} increase, and hence, V_{parent} decreases. After the plug splits, $t > 0.45$, each liquid volume becomes almost unchanged. Eventually, V_{upper} is smaller than V_{lower} because of the uneven split. The split ratio, R_S, can be calculated from the changes in liquid volume in each daughter tube before and after the plug splits

$$R_s = \frac{\Delta V_{upper}}{\Delta V_{lower}}. \tag{25}$$

ΔV_{upper} and ΔV_{lower} are increments of V_{upper} and V_{lower} after the split as shown in Fig. 9. $R_S = 1$ means an even split. $R_S = 0$ when all the liquid goes to the lower branch.

C. Effect of Bo

The split ratio, R_S, vs capillary number, $Ca = \mu_l \bar{U}/\sigma$, for three different $Bo = \rho_l g r_0^2/\sigma$ are plotted in Fig. 10. Symbols are the computational results, and dashed lines are calculated by Eq. (C1). Details on the extraction of Eq. (C1) are described in Appendix C. $\bar{U}$, which is used to calculate the computational Ca, is computed by averaging U
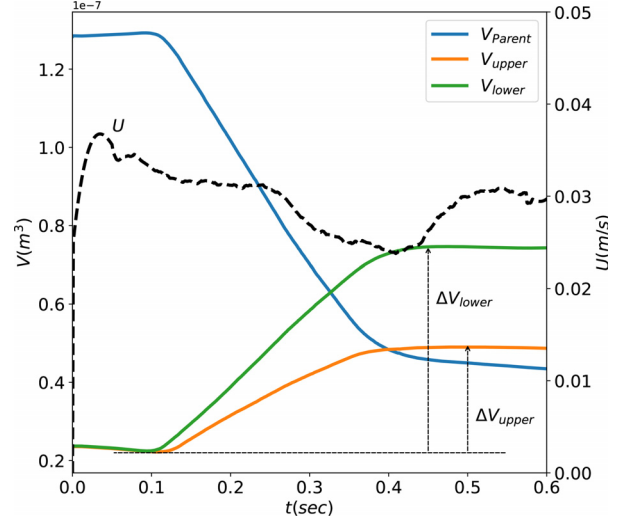

FIG. 9. A course of liquid volumes within the parent and daughter tubes, and the averaged air velocity in a cross section. V_{Parent} is the total liquid volume within $x < 3r_0$, while V_{upper} and V_{lower} are the total liquid volumes within $y \geq 0$ and $y < 0$ for $x \geq 3r_0$, respectively.

during plug splitting, for example, $0.1 < t < 0.45$ in the case shown in Fig. 9. U is the cross-sectional average velocity of air flow at $x = -3r_0$. Note that $x = 0$ is located at the point where the parent tube axis bifurcates, as shown in Fig. 2. Since the flow resistance of the plug varies depending on its configuration, U changes over time. As Bo increases, R_S decreases, implying that gravity leads to more liquid
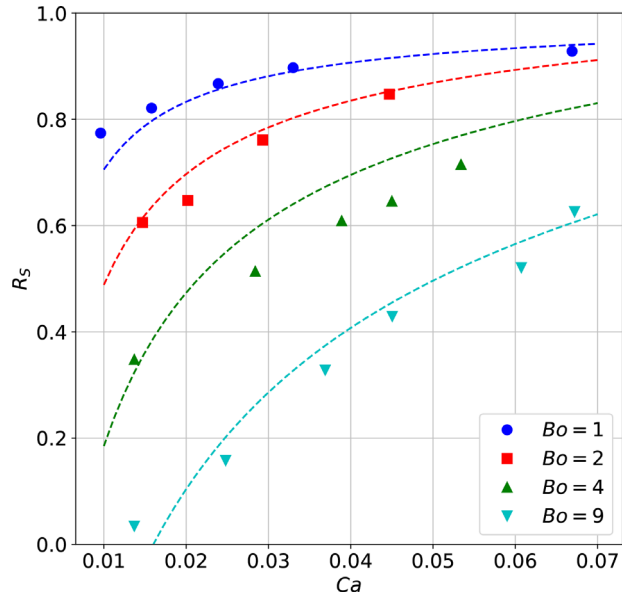

FIG. 10. The split ratio, R_S vs Ca. For $Bo = 1$, 4, and 9, $r_0 = 10^{-3}$, 2×10^{-3}, and 3×10^{-3} m, respectively, at a fixed $\sigma = 10^{-2}$ N/m. For $Bo = 2$, $r_0 = 2 \times 10^{-3}$ m and $\sigma = 2 \times 10^{-2}$ Pa m. Ca is calculated from the resultant plug speed, $\bar{U}$. Dashed lines are computed using Eq. (C1).

(a) $t = 0.6$ (sec)

(b) $t = 0.8$ (sec)

(c) $t = 0.9$ (sec)

(d) $t = 1.2$ (sec)
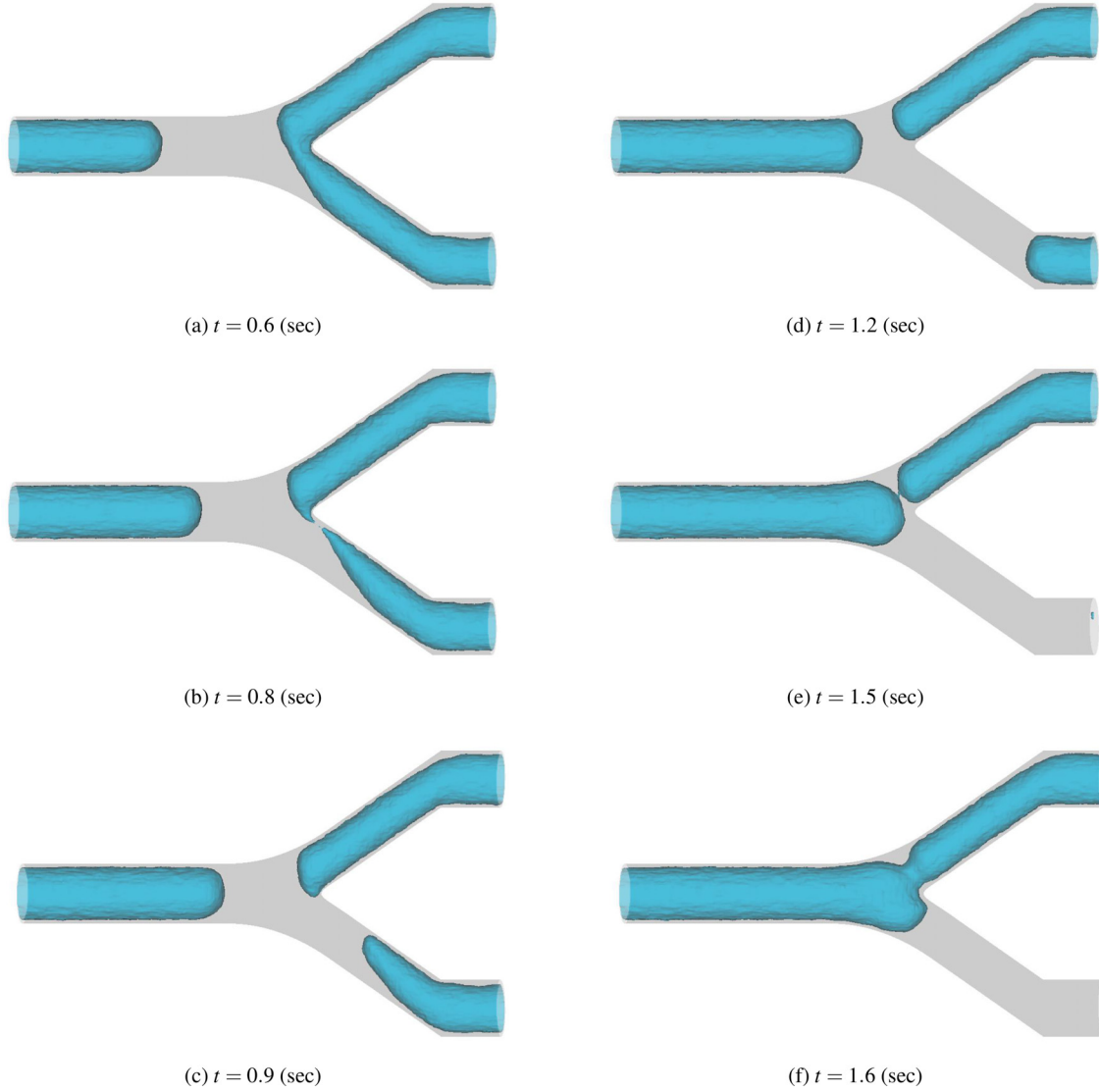
(e) $t = 1.5$ (sec)

(f) $t = 1.6$ (sec)

FIG. 11. Snapshots of a liquid plug splitting at a bifurcating tube. The inner surface of the bifurcating tube (gray) and the air–liquid interface (cyan) are plotted. $Bo = 9$, $La = 300$, $\theta_r = 90°$, $\theta_p = 0°$. The resultant $R_S = 0.0343$, $Ca = 0.0137$, and $Re = 4.11$. (a) $t = 0.6$ s, (b) $t = 0.8$ s, (c) $t = 0.9$ s, (d) $t = 1.2$ s, (e) $t = 1.5$ s, and (f) $t = 1.6$ s.

being delivered to the lower branch. It can be expected that $R_S \to 1$ as $Bo \to 0$ for any finite value of Ca. Increasing Ca, R_s also increases. The pressure difference due to the gravity becomes less significant as the overall pressure drop increases, which leads to a more symmetric splitting. These tendencies are consistent with previous studies.[37,38,43] It can be expected that $R_S \to 1$ as $Ca \to \infty$ for any finite value of Bo.

From the result presented in Fig. 10, in a fixed bifurcation geometry with stable surface tension and gravity, the split ratio of the plug will increase with increasing plug speed. Furthermore, at a fixed plug speed, when the surface tension increases, for example, $Ca = 0.06 \to 0.03$ and $Bo = 9 \to 4.5$, the split ratio of the plug will increase.

D. Critical Ca

For $Bo = 9$ at the smallest Ca in Fig. 10, the split ratio is close to zero, $R_S = 0.03$. Figure 11 demonstrates the plug-splitting process for this case. When the front interface of the plug moves into the bifurcating section, Fig. 11(a), the liquid already drains into the lower branch because of the strong gravitational effect. After the front interface is split, the two front interfaces deform to a hemisphere-shaped shape as a result of the surface tension. Due to the gravity, the plug portion in the lower daughter tube moves faster and the plug portion in the upper daughter tube is almost stagnant, as shown in Figs. 11(b)–11(d). When the rear interface of the plug enters the bifurcating section, the rear interface merges with the front interface at the upper daughter

tube. The plug that splits to the upper branch ruptures immediately. As discussed in previous studies,[37,43] there exists a critical capillary number, Ca_{crit}, such that for $Ca \leq Ca_{crit}$, the plug does not split into two daughter plugs, but one propagates into the lower daughter tube. Because the plug in the upper daughter tube propagates against the gravity, the driving pressure is required to overcome the hydrostatic pressure due to the gravity. Ca_{crit} will be decreased with Bo.

E. Effect of the roll and pitch angles

The effect of the roll and pitch angles on the split ratio is shown in Fig. 12. As the roll angle, θ_r decreases, R_S at a fixed Ca increases.
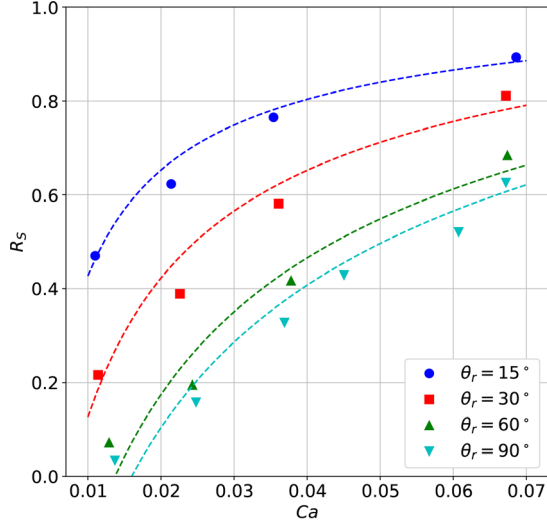
(a) Effect of roll angle, θ_r on R_S at a fixed pitch angle, $\theta_p=0°$.
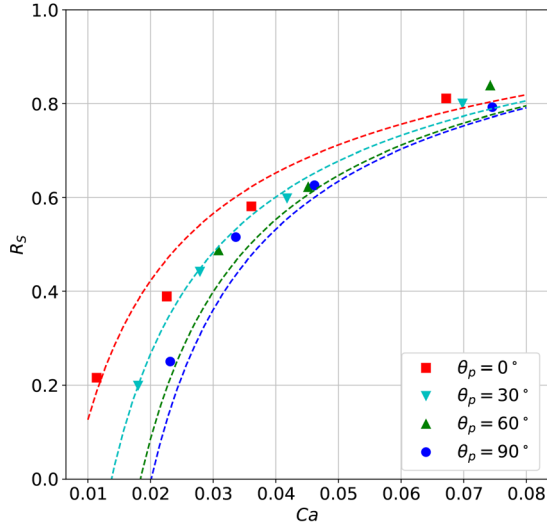
(b) Effect of pitch angle, θ_p on R_S at a fixed roll angle, $\theta_r=30°$.

FIG. 12. The split ratio, R_S vs Ca at $Bo=9$ for different roll and pitch angles. Dashed lines are computed using Eq. (C1). (a) Effect of roll angle, θ_r on R_S at a fixed pitch angle, $\theta_p=0°$. (b) Effect of pitch angle, θ_p on R_S at a fixed roll angle, $\theta_r=30°$.

When $\theta_r=0°$, $R_S=1$ for any Ca (not shown). The traverse component of gravity (y component, see Fig. 2) is $g \sin \theta_r$ referring to Eq. (7). Thus, the effective Bond number is $Bo \sin \theta_r$. Therefore, the overall trend is similar to that in Fig. 10. For the cases of $\theta_r=60°$ and $90°$, for $Ca < 0.015$, we observed that the plug entered into the upper daughter tube ruptured (similar to Fig. 11). For other roll angles, there must be a critical capillary number Ca_{crit} present, below which the plug does not split into two daughter plugs, but one propagates into the lower daughter tube. Ca_{crit} will decrease with the roll angle. The numerical results agree with the dashed lines, which are computed using Eq. (C1).

As Fig. 12(b) shows, the effect of the pitch angle, θ_p, on the split ratio is insignificant. Thinking about the gravity force by Eq. (7), when $\theta_r=90°$, θ_p does not change the gravity effect at all. When $\theta_r=90°$, as θ_p changes from $0°$ to $90°$, x and z components change, but y component is most dominant. For a small roll angle, $\theta_r < 90°$, the change in θ_p changes the local flow field and can cause a change in the plug split ratio, but it is not significant.

F. Effect of initial plug length

Figure 13 shows R_S vs Ca for three different initial plug lengths. The "semi-infinite" denotes a semi-infinitely long plug, where the front air–liquid interface is placed in the parent tube initially and moves into the air-filled bifurcating tube, followed by liquid with the absence of rear interface. As L_{P0} increases, R_S at a fixed Ca increases up to the value of semi-infinite. For $L_{P0}=2$, when $Ca < 0.04$, the plug in the upper daughter tube ruptures immediately after splitting and, when $Ca > 0.04$, the plugs in both daughter tubes rupture after splitting. The numerical results with finite L_{P0} agree with dashed lines, which are computed using Eq. (C1). For semi-infinite, the dashed line is computed setting $\Delta P_m = 0$, $\Delta P_b = 0$, and $h_0 = 0$. Equation (C1) predicts R_S of semi-infinite well for $Ca < 0.03$ but underestimates for $Ca > 0.03$.
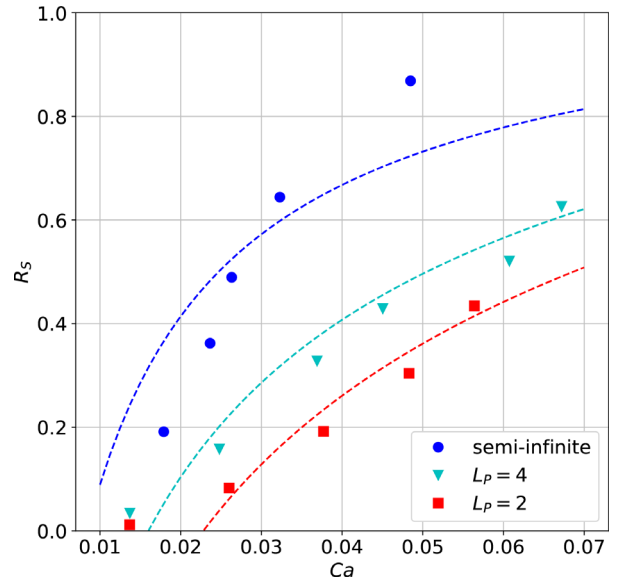

FIG. 13. The split ratio, R_S vs Ca at $Bo=9$ for different initial plug lengths. Semi-infinite denotes semi-finitely long plug. Dashed lines are computed using Eq. (C1).

G. Effect of inertia

The relation of Re to Ca can be written as $Re = La \cdot Ca$, where La is the Laplace number. Figure 14 shows the effect of La on the split ratio. As La increases, Re at a fixed Ca increases. Thus, the pressure loss at bifurcation increases with La. As Ca decreases, the impact on R_S by La becomes smaller because the inertial effect is less dominant for small $Re = La \cdot Ca$. At large Ca, R_S increases with La. Equation (C1) predicts well.

H. Comparison with experiments

Finally, we compare Eq. (C1) with the experimental data by Zheng et al.,[38] that is, shown in Fig. 15. Since the geometry differs from the numerical model in this study, the friction factor parameters were calculated based on the experimental data and were $A = 26.7$, $B = 16.8$ and $C = 0.50$. Equation (C1) agrees qualitatively well with the experimental data. The slope of the LB400X experimental data is smaller than in theory. Since the viscosity of LB400X is much larger than that of others, La is smaller than other test fluids as well as the range of our simulation. Therefore, our empirical formula may not predict the split ratio well for small La. This could cause a difference in slope.

IV. CONCLUSIONS AND FUTURE WORK

A particle method is presented to simulate the propagation of a liquid plug through an air-filled bifurcating tube. The method handles large deformation, break, and merge of the air–liquid interface. The singularity of the air–liquid interface is blurred by a model Dirac delta function with a finite peak; thus, the surface force caused by the surface tension is spread over a narrow transition region in the vicinity of the air–liquid interface. We successfully simulate the propagation of the liquid plug in a straight and bifurcating tube using the MPS method presented here. The present computational framework allows us to
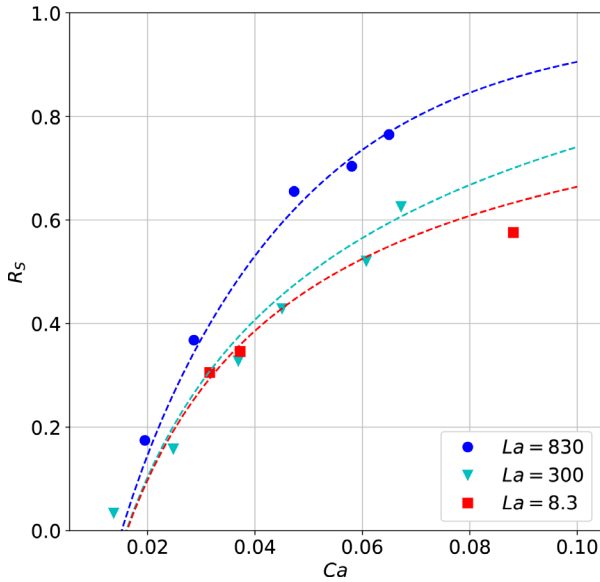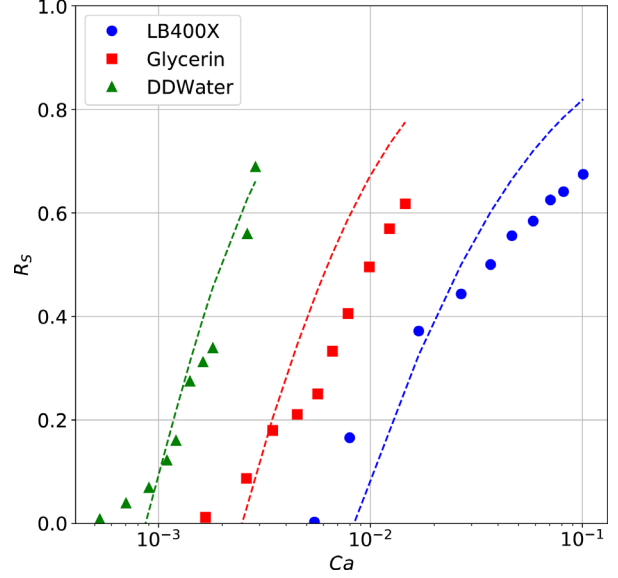

FIG. 15. The experimental results by Zheng et al.[38] The split ratio, R_S vs Ca for three different liquid materials. The roll angle, $\theta_r = 30°$, and the pitch angle, $\theta_p = 0°$. LB-400X: machine oil, $Bo = 1.26$, $La = 2.7$. Glycerin: 60% glycerin, $Bo = 0.67$, $La = 1.7 \times 10^3$. DDWater: de-ionized distilled water, $Bo = 0.54$, $La = 1.4 \times 10^5$. Dashed lines are computed using Eq. (C1). The parameters for the friction factor, Eq. (C2) are $A = 26.7$, $B = 16.8$, and $C = 0.40$.

perform simulations to understand the behavior of liquid plugs in pulmonary airways.

When the front meniscus of the plug splits at the bifurcation carina, the surface curvature becomes large, and the Laplace pressure accelerates the liquid near the wall. Due to the faster movement of the interface, the wall shear stress becomes large. This may cause damage to pulmonary epithelial cells.

We observed that the presence of a transverse gravitational force causes asymmetries in plug splitting; gravity leads to more liquid being delivered to the lower branch. We calculate the split ratio, R_S, which is the ratio of liquid volume in two daughter tubes after the plug split. We show that R_S decreases, which means a more uneven split, as Ca decreases at a fixed Bo. Also, we show that R_S decreases as Bo increases at a fixed Ca. The results agree with previous experimental and computational studies.[37,38,43] We also observed that there exists a critical capillary number in which the plug does not split into two daughter plugs but instead propagates into the lower daughter tube. This is due to the existence of a minimal driving pressure, which is required to overcome the hydrostatic pressure due to gravity.

In SRT or drug delivery in lungs, faster plug speed, which yields a large Ca, will result in more uniform split in airway bifurcation. However, since the trailing film thickness of the plugs increases with Ca, the plugs lose mass faster. Therefore, there must be an optimal plug speed to deliver the liquid uniformly to the distal airways. In small airways, since Bo is small, the gravity effect will be less significant.

In this study, we focus on a symmetrical and plane bifurcating tube. In future work, we will explore a larger parameter space, including asymmetric and/or non-plane bifurcation geometries, which can

FIG. 14. The split ratio, R_S vs Ca at $Bo = 9$ for different Laplace number, La. Dashed lines are computed using Eq. (C1).

be built by tweaking the parameters defined in Appendix A. The effect of surfactant on the split of the liquid plug will be investigated using the method presented in the previous study,[59] where we need to solve two transport equations for surfactant in the bulk fluid and at the interface. Through these future investigations, we will refine the simple reduced-dimension model of the split of the plug, which contributes to achieving a better understanding of how to use liquid plugs effectively in medical treatment and how a plug behaves once it is created.[40,60]

AUTHOR DECLARATIONS
Conflict of Interest

The authors have no conflicts to disclose.

Author Contributions

Hideki Fujioka: Conceptualization (equal), Data curation (equal), Formal analysis (equal), Investigation (lead), Methodology (lead), Project administration (equal), Software (lead), Supervision (equal), Validation (equal), Visualization (lead), and Writing – original draft (lead). **Francesco Romanò:** Conceptualization (equal), Data curation (equal), Formal analysis (equal), Investigation (equal), Project administration (equal), and Writing – review and editing (equal). **Metin Muradoglu:** Conceptualization (equal), Data curation (equal), Formal analysis (equal), Investigation (equal), Project administration (equal), and Writing – review and editing (equal). **James B. Grotberg:** Conceptualization (equal), Data curation (equal), Formal analysis (equal), Funding acquisition (lead), Investigation (equal), Project administration (equal), and Writing – review and editing (equal).

DATA AVAILABILITY

The data that support the findings of this study are available from the corresponding author upon reasonable request.

APPENDIX A: BIFURCATION MODEL

In this study, we construct a realistic model of airway bifurcation, which has a smooth curved surface, particularly at the flow divider.[49] The curved line is defined as the tube axis, which provides a density space around the axis like a magnetic flux density around an electronic wire. Here, the bifurcating tube model is built, defining two tube axes, $\mathbf{x}_1$ and $\mathbf{x}_2$, as sketched in Fig. 2. These two axes provide the density space around the axis for a given position, $\mathbf{x}$, as

$$H_1 = \frac{G_1(\tilde{\mathbf{x}}_1)}{||\tilde{\mathbf{x}}_1 - \mathbf{x}||} \quad \text{and} \quad H_2 = \frac{G_2(\tilde{\mathbf{x}}_2)}{||\tilde{\mathbf{x}}_2 - \mathbf{x}||}, \tag{A1}$$

where $\tilde{\mathbf{x}}_1$ and $\tilde{\mathbf{x}}_2$ are the closest points from $\mathbf{x}$ to axes $\mathbf{x}_1$ and $\mathbf{x}_2$, respectively. The model surface is the summation of nth powers of these density spaces provided by Eq. (A1) being unity

$$\mathcal{H} = H_1{}^n + H_2{}^n = 1, \tag{A2}$$

where n is a parameter to control the sharpness of the flow divider. Large n yields a sharp flow divider shape. In this study, $n = 4$ is used.

The axes of the bifurcating tube can be divided into three regions, which are the parent tube, the central zone, and the daughter tubes. The two central axes merge into a single straight line of the parent tube. $G_1(\tilde{\mathbf{x}}_1)$ and $G_2(\tilde{\mathbf{x}}_2)$ are functions that determine the radius of the tube. Scaling with r_0, $G_1(\tilde{\mathbf{x}}_1)$ is defined for each region as

$$G_1(\tilde{\mathbf{x}}_1) = \begin{cases} \left(\frac{1}{2}\right)^{\frac{1}{n}}, & \text{parent tube,} \\[2mm] \left(\frac{1}{2}\right)^{\frac{1}{n}} + \left\{\frac{r_1}{r_0} - \left(\frac{1}{2}\right)^{\frac{1}{n}}\right\}\frac{\angle(\tilde{\mathbf{x}}_1)}{\theta_1}, & \text{central zone,} \\[2mm] \frac{r_1}{r_0}, & \text{daughter tube,} \end{cases} \tag{A3}$$

where $\angle(\tilde{\mathbf{x}}_1)$ denotes the angle of $\tilde{\mathbf{x}}_1$ from x axis with respect to the center of each curve, thus $0 \leq \angle(\tilde{\mathbf{x}}_1) < \theta_1$. $G_2(\tilde{\mathbf{x}}_2)$ can be defined similarly. For a given coordinate, $\mathbf{x}$, when $\mathcal{H} > 1$, $\mathbf{x}$ is inside the tube. When $\mathcal{H} < 1$, $\mathbf{x}$ is outside the tube. The unit normal on the wall can be calculated by $\mathbf{n} = -\nabla\mathcal{H}/||\nabla\mathcal{H}||$, and the mean curvature can be calculated by $\kappa = \nabla \cdot \mathbf{n}$.

APPENDIX B: DISCRETE FORM OF SPATIAL DERIVATIVES

In the MPS method,[48] the spatial derivatives are discretized using the distributed particles and their properties. The derivatives of each variable are calculated from the values owned by the particles. The gradient of a scalar ϕ at particle i is defined by

$$\nabla\phi_i = \frac{d}{\psi_i} \sum_{j \neq i} \frac{\phi_j - \phi_i}{||\mathbf{x}_j - \mathbf{x}_i||^2}(\mathbf{x}_j - \mathbf{x}_i)w(||\mathbf{x}_j - \mathbf{x}_i||), \tag{B1}$$

the divergence of a vector $\mathbf{v}$ is defined by

$$\nabla \cdot \mathbf{v}_i = \frac{d}{\psi_i} \sum_{j \neq i} \frac{(\mathbf{v}_j - \mathbf{v}_i) \cdot (\mathbf{x}_j - \mathbf{x}_i)}{||\mathbf{x}_j - \mathbf{x}_i||^2}w(||\mathbf{x}_j - \mathbf{x}_i||), \tag{B2}$$

the Laplacian of a scalar or vector ϕ is defined by

$$\nabla^2\phi_i = \frac{2d}{\lambda\psi_i} \sum_{j \neq i} \left[(\phi_j - \phi_i)w(||\mathbf{x}_j - \mathbf{x}_i||)\right], \tag{B3}$$

where d is the dimensions of the space, i.e., for the three-dimensional case, $d = 3$ as it in the present study, and λ is defined as

$$\lambda = \frac{\sum_{j \neq i} ||\mathbf{x}_j - \mathbf{x}_i||^2 w(||\mathbf{x}_j - \mathbf{x}_i||)}{\sum_{j \neq i} w(||\mathbf{x}_j - \mathbf{x}_i||)}. \tag{B4}$$

APPENDIX C: SIMPLE MODEL OF PLUG SPLIT RATIO

A simple model is developed to investigate the plug splitting process in a similar way to Zheng *et al.*[37] For simplification, the curved tubes of the bifurcation model are replaced by straight tubes.

The motion of the plug is considered quasi-steady, and the expression for the split ratio, R_S, is derived by a theoretical calculation of the pressure drops and mass balances between the parent and daughter tubes. We did not focus on the effect of gravity on the shape of the meniscus of the air–liquid interface, as previously studied by Suresh and Grotberg.[25] The pressure drop between the parent and daughter tubes has different contributions. It includes the capillary jump across the air–liquid interfaces, the viscous dissipation, and the gravitational hydrostatic effect. The balance of pressure drops in the plug is simplified as[37]

$$
\underbrace{4\left(\frac{r_0}{L_{P0}}\right)\left(\frac{r_1}{r_0}\right)\left[\tilde{f}_2(3Ca_2)^{2/3} - \tilde{f}_1(3Ca_1)^{2/3}\right](R_S + 1)}_{\Delta P_m}
$$
$$
+ \underbrace{\mathscr{F}Ca\left[1 - \left(\frac{h_0}{r_0}\right)\right]^2\left(\frac{r_1}{r_0}\right)^{-4}(R_S - 1)}_{\Delta P_v}
$$
$$
+ \underbrace{4\left(\frac{r_0}{L_{P0}}\right)\left(\frac{r_1}{r_0}\right)^3 Bo\cos\theta_1\sin\theta_r(R_S + 1)}_{\Delta P_b}
$$
$$
+ \underbrace{Bo\sin\theta_1\sin\theta_r(R_S + 1)}_{\Delta P_r}
$$
$$
- \underbrace{Bo\cos\theta_1\cos\theta_r\sin\theta_p(R_S - 1)}_{\Delta P_p} = 0. \qquad (C1)
$$

The first term, ΔP_m, is due to the pressure drop across the front menisci of plugs in the daughter tubes. The second term, ΔP_v, is due to the viscous dissipation, and $\mathscr{F}$ is the friction factor. The third term, ΔP_b, is due to the hydrostatic pressure difference between the entrances of daughter tubes. The forth term, ΔP_r, is due to the hydrostatic pressure as a function of the roll angle, θ_r. The fifth term, ΔP_p, is due to the hydrostatic pressure as a function of the pitch angle, θ_p. Equation (C1) remains implicit form because Ca_1 and Ca_2 are function of R_S. Thus, to obtain R_S, we need to solve Eq. (C1) for R_S numerically.

Dashed lines in Fig. 10 are computed using Eq. (C1) with the precursor film thickness of $h_1/r_1 = 0.05$ and the initial plug length of $L_{P0} = 4$. Considering the large pressure loss across the bifurcation, we define the friction factor, $\mathscr{F}$, is a function of the Reynolds number, $Re = La \cdot Ca = \rho_l r_0 \bar{U}/\mu_l$, as

$$
\mathscr{F} = A + B \cdot Re^C. \qquad (C2)
$$

From a curve-fitting analysis, we obtain $A = 229$, $B = 0.0638$, and $C = 2.11$, which make approximately 30 times of the same factor for the Poiseuille flow that is $\mathscr{F} = 8$ and show excellent agreement with our MPS simulation results as lines and corresponding markers agree well for all the Bo considered, see Fig. 10. Comparing each term in Eq. (C1), $\Delta P_p = 0$ since $\theta_p = 0°$, and ΔP_m is negligibly small, thus the contribution of the pressure jump across the front interfaces is negligible. The first term will become significant by shorter plugs, asymmetric bifurcations, and the presence of surfactant on the air–liquid interface.

Our numerical results show that the contribution of ΔP_m and ΔP_p terms in Eq. (C1) to the split ratio is small. Neglecting two terms, we can simplify Eq. (C1) and make it an explicit form as

$$
R_S = \frac{\Delta P_v - \Delta P_b - \Delta P_r}{\Delta P_v + \Delta P_b + \Delta P_r}. \qquad (C3)
$$

REFERENCES

[1] W. Long, T. Thompson, H. Sundell, R. Schumacher, F. Volberg, R. Guthrie, A. E. N. S. Group et al., "Effects of two rescue doses of a synthetic surfactant on mortality rate and survival without bronchopulmonary dysplasia in 700-to 1350-gram infants with respiratory distress syndrome," J. Pediatr. **118**, 595–605 (1991).

[2] H. Yapıcıoğlu, D. Y. ild izdaş, İ. Bayram, Y. Sertdemir, and H. L. Y. ilmaz, "The use of surfactant in children with acute respiratory distress syndrome: Efficacy in terms of oxygenation, ventilation and mortality," Pulm. Pharmacol. Ther. **16**, 327–333 (2003).

[3] M. Salvia-Roigés, X. Carbonell-Estrany, J. Figueras-Aloy, and J. Rodríguez-Miguélez, "Efficacy of three treatment schedules in severe meconium aspiration syndrome," Acta Paediatr. **93**, 60–65 (2004).

[4] S. M. Donn and J. Dalton, "Surfactant replacement therapy in the neonate: Beyond respiratory distress syndrome," Respir. Care **54**, 1203–1208 (2009); available online at https://rc.rcjournal.com/content/54/9/1203/tab-article-info.

[5] M.-J. Jeng, W.-J. Soong, and Y.-S. Lee, "Effective lavage volume of diluted surfactant improves the outcome of meconium aspiration syndrome in newborn piglets," Pediatr. Res. **66**, 107 (2009).

[6] J. B. Grotberg, M. Filoche, D. F. Willson, K. Raghavendran, and R. H. Notter, "Did reduced alveolar delivery of surfactant contribute to negative results in adults with acute respiratory distress syndrome?," Am. J. Respir. Crit. Care Med. **195**, 538–540 (2017).

[7] R. B. Hirschl, M. Croce, D. Gore, H. Wiedemann, K. Davis, J. Zwischenberger, and R. H. Bartlett, "Prospective, randomized, controlled pilot study of partial liquid ventilation in adult acute respiratory distress syndrome," Am. J. Respir. Crit. Care Med. **165**, 781–787 (2002).

[8] P. N. Cox, H. Frndova, O. Karlsson, S. Holowka, and C. A. Bryan, "Fluorocarbons facilitate lung recruitment," Intensive Care Med. **29**, 2297–2302 (2003).

[9] K. Mikawa, K. Nishina, Y. Takao, and H. Obara, "Efficacy of partial liquid ventilation in improving acute lung injury induced by intratracheal acidified infant formula: Determination of optimal dose and positive end-expiratory pressure level," Crit. Care Med. **32**, 209–216 (2004).

[10] Z.-L. Guo, G.-P. Lu, T. Ren, Y.-H. Zheng, J.-Y. Gong, J. Yu, and Y.-J. Liang, "Partial liquid ventilation confers protection against acute lung injury induced by endotoxin in juvenile piglets," Respir. Physiol. Neurobiol. **167**, 221–226 (2009).

[11] S. Rasche, S. Friedrich, J. U. Bleyl, M. Gama de Abreu, T. Koch, and M. Ragaller, "Pilot study of vaporization of perfluorohexane during high-frequency oscillatory ventilation in experimental acute lung injury," Exp. Lung Res. **36**, 538–547 (2010).

[12] O. E. Jensen, D. Halpern, and J. B. Grotberg, "Transport of a passive solute by surfactant-driven flows," Chem. Eng. Sci. **49**, 1107–1117 (1994).

[13] J. Yu and Y. W. Chien, "Pulmonary drug delivery: Physiologic and mechanistic aspects," Crit. Rev. Ther. Drug Carrier Syst. **14**, 395–453 (1997).

[14] Y. L. Zhang, O. K. Matar, and R. V. Craster, "A theoretical study of chemical delivery within the lung using exogenous surfactant," Med. Eng. Phys. **25**, 115–132 (2003).

[15] S. Iqbal, S. Ritson, I. Prince, J. Denyer, and M. L. Everard, "Drug delivery and adherence in young children," Pediatr. Pulmonol. **37**, 311–317 (2004).

[16] P. B. Myrdal, K. L. Karlage, S. W. Stein, B. A. Brown, and A. Haynes, "Optimized dose delivery of the peptide cyclosporine using hydrofluoroalkane-based metered dose inhalers," J. Pharm. Sci. **93**, 1054–1061 (2004).

[17] F. F. Espinosa and R. D. Kamm, "Meniscus formation during tracheal instillation of surfactant," J. Appl. Physiol. **85**, 266–272 (1998).

[18] K. J. Cassidy, J. L. Bull, M. R. Glucksberg, C. A. Dawson, S. T. Haworth, R. Hirschl, N. Gavriely, and J. B. Grotberg, "A rat lung model of instilled liquid transport in the pulmonary airways," J. Appl. Physiol. **90**, 1955–1967 (2001).

[19] J. C. Anderson, R. C. Molthen, C. A. Dawson, S. T. Haworth, J. L. Bull, M. R. Glucksberg, and J. B. Grotberg, "Effect of ventilation rate on instilled surfactant distribution in the pulmonary airways of rats," J. Appl. Physiol. **97**, 45–56 (2004).

[20]J. L. Bull, S. Tredici, E. Komori, D. O. Brant, J. B. Grotberg, and R. B. Hirschl, "Distribution dynamics of perfluorocarbon delivery to the lungs: An intact rabbit model," J. Appl. Physiol. **96**, 1633–1642 (2004).

[21]J. B. Grotberg, "Crackles and wheezes: Agents of injury?," Ann. Am. Thorac. Soc. **16**, 967–969 (2019).

[22]P. G. Gibson, L. Qin, and S. H. Puah, "Covid-19 acute respiratory distress syndrome (ARDS): Clinical features and differences from typical pre-covid-19 ARDS," Med. J. Aust. **213**, 54–56 (2020).

[23]P. D. Howell, S. L. Waters, and J. B. Grotberg, "The propagation of a liquid bolus along a liquid-lined flexible tube," J. Fluid Mech. **406**, 309–335 (2000).

[24]S. L. Waters and J. B. Grotberg, "The propagation of a surfactant laden liquid plug in a capillary tube," Phys. Fluids **14**, 471–480 (2002).

[25]V. Suresh and J. B. Grotberg, "The effect of gravity on liquid plug propagation in a two-dimensional channel," Phys. Fluids **17**, 031507 (2005).

[26]S. S. Mamba, J. Magniez, F. Zoueshtiagh, and M. Baudoin, "Dynamics of a liquid plug in a capillary tube under cyclic forcing: Memory effects and airway reopening," J. Fluid Mech. **838**, 165–191 (2018).

[27]H. Fujioka and J. B. Grotberg, "Steady propagation of a liquid plug in a two-dimensional channel," J. Biomech. Eng. **126**, 567–577 (2004).

[28]H. Fujioka and J. B. Grotberg, "The steady propagation of a surfactant-laden liquid plug in a two-dimensional channel," Phys. Fluids **17**, 082102 (2005).

[29]Y. Zheng, H. Fujioka, and J. B. Grotberg, "Effects of gravity, inertia, and surfactant on steady plug propagation in a two-dimensional channel," Phys. Fluids **19**, 082107 (2007).

[30]H. Fujioka, S. Takayama, and J. B. Grotberg, "Unsteady propagation of a liquid plug in a liquid-lined straight tube," Phys. Fluids **20**, 062104 (2008).

[31]D. M. Campana, S. Ubal, M. D. Giavedoni, and F. A. Saita, "Stability of the steady motion of a liquid plug in a capillary tube," Ind. Eng. Chem. Res. **46**, 1803–1809 (2007).

[32]P. Zamankhan, B. T. Helenbrook, S. Takayama, and J. B. Grotberg, "Steady motion of Bingham liquid plugs in two-dimensional channels," J. Fluid Mech. **705**, 258–279 (2012).

[33]E. A. Hassan, E. Uzgoren, H. Fujioka, J. B. Grotberg, and W. Shyy, "Adaptive Lagrangian–Eulerian computation of propagation and rupture of a liquid plug in a tube," Int. J. Numer. Methods Fluids **67**, 1373–1392 (2011).

[34]M. Muradoglu, F. Romanò, H. Fujioka, and J. B. Grotberg, "Effects of surfactant on propagation and rupture of a liquid plug in a tube," J. Fluid Mech. **872**, 407–437 (2019).

[35]B. He, C. Qin, W. Chen, and B. Wen, "Numerical simulation of pulmonary airway reopening by the multiphase lattice Boltzmann method," Comput. Math. Appl. **108**, 196–205 (2022).

[36]F. Romanò, H. Fujioka, M. Muradoglu, and J. B. Grotberg, "Liquid plug formation in an airway closure model," Phys. Rev. Fluids **4**, 093103 (2019).

[37]Y. Zheng, J. C. Anderson, V. Suresh, and J. B. Grotberg, "Effect of gravity on liquid plug transport through an airway bifurcation model," J. Biomech. Eng. **127**, 798–806 (2005).

[38]Y. Zheng, H. Fujioka, J. C. Grotberg, and J. B. Grotberg, "Effects of inertia and gravity on liquid plug splitting at a bifurcation," J. Biomech. Eng. **128**, 707–716 (2006).

[39]A. Copploe, M. Vatani, R. Amini, J.-W. Choi, and H. Tavana, "Engineered airway models to study liquid plug splitting at bifurcations: Effects of orientation and airway size," J. Biomech. Eng. **140**, 091012 (2018).

[40]M. Filoche, C.-F. Tai, and J. B. Grotberg, "Three-dimensional model of surfactant replacement therapy," Proc. Natl. Acad. Sci. **112**, 9287–9292 (2015).

[41]C.-F. Tai, B. L. Vaughan, M. Florens, M. Filoche, and J. B. Grotberg, "Liquid and drug delivery into a 3d lung tree," in *Proceedings of the A98. Computational Models of the Lung: What Do They Give US?* (American Thoracic Society, 2011), p. A2298.

[42]A. Kazemi, B. Louis, D. Isabey, G. F. Nieman, L. A. Gatto, J. Satalin, S. Baker, J. B. Grotberg, and M. Filoche, "Surfactant delivery in rat lungs: Comparing 3d geometrical simulation model with experimental instillation," PLoS Comput. Biol. **15**, e1007408 (2019).

[43]B. L. Vaughan and J. B. Grotberg, "Splitting of a two-dimensional liquid plug at an airway bifurcation," J. Fluid Mech. **793**, 1–20 (2016).

[44]S. O. Unverdi and G. Tryggvason, "A front-tracking method for viscous, incompressible, multi-fluid flows," J. Comput. Phys. **100**, 25–37 (1992).

[45]G. Tryggvason, B. Bunner, A. Esmaeeli, D. Juric, N. Al-Rawahi, W. Tauber, J. Han, S. Nas, and Y.-J. Jan, "A front-tracking method for the computations of multiphase flow," J. Comput. Phys. **169**, 708–759 (2001).

[46]C. W. Hirt and B. D. Nichols, "Volume of fluid (VOF) method for the dynamics of free boundaries," J. Comput. Phys. **39**, 201–225 (1981).

[47]J. A. Sethian, *Level Set Methods and Fast Marching Methods: Evolving Interfaces in Computational Geometry, Fluid Mechanics, Computer Vision, and Materials Science* (Cambridge University Press, 1999), Vol. 3.

[48]S. Koshizuka and Y. Oka, "Moving-particle semi-implicit method for fragmentation of incompressible fluid," Nucl. Sci. Eng. **123**, 421–434 (1996).

[49]T. J. Pedley, "Pulmonary fluid dynamics," Annu. Rev. Fluid Mech. **9**, 229–274 (1977).

[50]T. Heistracher and W. Hofmann, "Physiologically realistic models of bronchial airway bifurcations," J. Aerosol Sci. **26**, 497–509 (1995).

[51]J. U. Brackbill, D. B. Kothe, and C. Zemach, "A continuum method for modeling surface tension," J. Comput. Phys. **100**, 335–354 (1992).

[52]A. M. Gambaruto, "Computational haemodynamics of small vessels using the moving particle semi-implicit (MPS) method," J. Comput. Phys. **302**, 68–96 (2015).

[53]S. Balay, W. D. Gropp, L. C. McInnes, and B. F. Smith, "Efficient management of parallelism in object oriented numerical software libraries," in *Modern Software Tools in Scientific Computing*, edited by E. Arge, A. M. Bruaset, and H. P. Langtangen (Birkhäuser Press, 1997), pp. 163–202.

[54]G. Guennebaud, B. Jacob *et al.*, see http://eigen.tuxfamily.org for "Eigen v3, 2010."

[55]The HDF Group, see https://www.hdfgroup.org/HDF5/ for "Hierarchical Data Format, version 5, 1997–2020."

[56]E. R. Weibel, A. F. Cournand, and D. W. Richards, *Morphometry of the Human Lung* (Springer, 1963), Vol. 1.

[57]D. Halpern and D. P. Gaver III, "Boundary element analysis of the time-dependent motion of a semi-infinite bubble in a channel," J. Comput. Phys. **115**, 366–375 (1994).

[58]D. Huh, H. Fujioka, Y.-C. Tung, N. Futai, R. Paine, J. B. Grotberg, and S. Takayama, "Acoustically detectable cellular-level lung injury induced by fluid mechanical stresses in microfluidic airway systems," Proc. Natl. Acad. Sci. **104**, 18886–18891 (2007).

[59]H. Fujioka, "A continuum model of interfacial surfactant transport for particle methods," J. Comput. Phys. **234**, 280–294 (2013).

[60]J. Ryans, H. Fujioka, D. Halpern, and D. P. Gaver III, "Reduced-dimension modeling approach for simulating recruitment/de-recruitment dynamics in the lung," Ann. Biomed. Eng. **44**, 3619–3631 (2016).